A&A 572, L4 (2014)
DOI: 10.1051/0004-6361/201424607
© ESO 2014

Astronomy & Astrophysics

Letter to the Editor

Dust correction factors over 0 < z < 3 in massive star-forming galaxies derived from a stacking analysis of *Herschel* data⋆,⋆⋆

I. Oteo[1,2]

[1] Institute for Astronomy, University of Edinburgh, Royal Observatory, Blackford Hill, Edinburgh EH9 3HJ, UK
e-mail: ivanoteogomez@gmail.com
[2] European Southern Observatory, Karl-Schwarzschild-Str. 2, 85748 Garching, Germany

Received 15 July 2014 / Accepted 4 September 2014

ABSTRACT

We use a stacking analysis in *Herschel*/PACS to study the accuracy of several dust-correction factors that are typically employed to estimate the total star-formation rate (SFR) of high-redshift, massive, star-forming (SF) galaxies. We also analyze what stacking suggests about the relation between SFR and stellar mass and the redshift evolution of the specific SFR ($sSFR = SFR/M_*$). We find that the dust properties of massive SF galaxies evolve with redshift, that is, galaxies at $z \sim 2$–3 are more attenuated than at $z \sim 1$ for a given UV continuum slope and stellar mass. As a consequence, a single IRX-β or dust-mass relation cannot be used to recover the total SFR of massive SF galaxies at $0 \lesssim z \lesssim 3$. This might have implications for studies at higher redshifts, where a single IRX-β relation derived for local starbursts is usually assumed to be valid. However, we find evidence that the local relations might be valid at least up to $z \sim 1$, where bluer and less massive galaxies can be detected through stacking. The spectral energy distribution fitting procedure with stellar population templates gives overestimated values (about 0.3–0.5 dex in $\log SFR$) of the dust-corrected SFR at all redshifts studied here. We find that the slope of the main-sequence of star formation is flatter than previously found in massive galaxies with $\log(M_*/M_\odot) \geq 10$, and the redshift evolution of the sSFR reported in previous works in massive galaxies is well recovered.

Key words. galaxies: photometry – galaxies: evolution – galaxies: high-redshift – galaxies: star formation

1. Introduction

To estimate dust attenuation and total star-formation rate (SFR) of star-forming (SF) galaxies at different redshifts several recipes have been traditionally employed in the literature when far-IR (FIR) information is not available. These include the IRX-β relation derived for local starburst (SB; Meurer et al. 1999) or using properties derived using ultraviolet (UV), optical, and/or near-IR (NIR) spectral energy distribution (SED) fits that do not include FIR data. However, there is increasing evidence that the dust properties of massive SF galaxies might have evolved with redshift and that local relations cannot be applied to high-redshift or special types of galaxies (Goldader et al. 2002; Oteo et al. 2013b).

Most previous analyses of dust correction factors in SF galaxies are based on direct detections in *Herschel* (Pilbratt et al. 2010) bands (Buat et al. 2010; Wuyts et al. 2011; Oteo et al. 2014). In fact, the most accurate values of dust attenuation and total SFR are those derived with individual detections in the FIR. Unfortunately, for a given redshift slice, only a small fraction of galaxies (those with the highest total SFRs) can be individually detected by *Herschel* even in the deepest surveys (Magdis et al. 2010; Rigopoulou et al. 2010; Heinis et al. 2013; Oteo et al. 2013c,b, 2014). Furthermore, a significant population of the high-redshift galaxies detected by *Herschel* are SB and not normal SF galaxies (see, for example, Rodighiero et al. 2014). Therefore, we need to rely on stacking analysis to study less extreme sources. In this work we study the accuracy of several dust-correction factors (IRX-β relation, dust-mass correlation, and SED fits) at different redshifts from a stacking analysis of *Herschel*/PACS-160 μm data (Poglitsch et al. 2010). We also explore what stacking indicates about the relation between SFR and stellar mass in massive SF galaxies and about the redshift evolution of the specific SFR (sSFR). This paper is organized as follows: Sect. 2 explains the source selection and the methodology. The main results are presented in Sect. 3. Finally, we summarize our main conclusions in Sect. 4. Throughout the paper, we assume a flat Universe with $(\Omega_m, \Omega_\Lambda, h_0) = (0.3, 0.7, 0.7)$, and all magnitudes are listed in the AB system (Oke & Gunn 1983).

2. Source selection and methodology

We focused on the COSMOS field (Scoville et al. 2007) and selected all rest-frame UV-selected sources whose photometric redshifts (taken from Ilbert et al. 2013) are within $0.02 \leq z \leq 4.0$. We avoided active galactic nucleus contamination by discarding all galaxies detected in X-rays (Elvis et al. 2009). We are interested here in SF galaxies. Different ways of selecting SF galaxies have been proposed in the literature, mostly based on single and double colors (Williams et al. 2009; Rodighiero et al. 2010). However, a single color-cut might exclude SF galaxies with red rest-frame $U - V$ colors (see Fig. 11 in Williams et al. 2009). Furthermore, red SF galaxies might occupy the green valley or even the red sequence of the color-magnitude diagram of galaxies (Oteo et al. 2014). Since SF galaxies are galaxies that form stars, we selected SF galaxies according to their SFR. In this way, we considered only galaxies whose SFR_{UV} (not corrected for dust attenuation) is at least 1 $M_\odot\,yr^{-1}$. This is a conservative approach, since a high percentage of low-redshift galaxies have an SFR higher than that threshold (Elbaz et al. 2007), and

⋆ *Herschel* is an ESA space observatory with science instruments provided by European-led Principal Investigator consortia and with important participation from NASA.
⋆⋆ Appendix A is available in electronic form at http://www.aanda.org

SF galaxies with $SFR \geq 1\ M_{\odot}\,\mathrm{yr}^{-1}$ can be detected at the highest redshifts studied in this work with the depth of the data we have used. We also compared our results with those derived by adopting a threshold $SFR_{\mathrm{UV}} \geq 5\ M_{\odot}\ \mathrm{yr}^{-1}$ at $z \geq 1$. Note that since these limits are before any dust correction, the actual SFR would be even higher.

The UV-to-NIR SEDs of the galaxies were fitted with Bruzual & Charlot (2003) templates to obtain their stellar mass, UV continuum slope (β), and rest-frame UV luminosity (L_{UV}) (see, for example, Oteo et al. 2013a). Templates associated with constant SFR and $Z = 0.2\ Z_{\odot}$ metallicity were considered. Dust attenuation was included with the Calzetti et al. (2000) law. We included intergalactic-medium absorption adopting the prescription of Madau (1995). Optical and NIR photometric information was taken from Ilbert et al. (2013), while GALEX data were taken from Zamojski et al. (2007) for galaxies at $z \leq 1$. The SED fits were made out with the Zurich Extragalactic Bayesian Redshift Analyzer (ZEBRA, Feldmann et al. 2006) code.

Since most of the galaxies are undetected by *Herschel* we must rely on a stacking analysis to estimate the FIR emission of UV-selected galaxies. To this aim we used the IAS stacking library (Béthermin et al. 2010) and focused on the PACS-160 μm band. We checked that stacking in PACS-100 μm gives similar results (see also Rodighiero et al. 2010). We stacked in the residual images, and median stacked images were considered. Only *Herschel*-undetected galaxies were considered in the stacking analysis. The stacked fluxes were obtained with a PSF-fitting procedure, and their uncertainties were calculated with a bootstrap analysis. We studied the effect of clustering (Béthermin et al. 2012) by comparing the PSF of PACS-160 μm with the actual radial profile of each stacked detection. This is similar to the method used in Heinis et al. (2013; see also method C in Béthermin et al. 2012). We compared the profile of the stacked detections and of the PSF of the PACS-160 μm observations, but found no additional broadening of the stacked emission because of clustering of the input catalog. Therefore, we did not include an additional correction (Magnelli et al. 2014). Radial profiles and stacked images are shown in Appendix A for stacks as a function of the UV continuum slope and stellar mass (see below). The PACS-160 μm were converted in total IR luminosities (L_{IR}) with single-band extrapolations using the templates of Chary & Elbaz (2001). This step provides a good estimate of L_{IR} since PACS-160 μm samples the dust emission peak at the redshift range of the galaxies studied. The stacked total SFR were obtained from luminosities with the Kennicutt (1998) relations and adopting $SFR_{\mathrm{total}} = SFR_{\mathrm{UV}} + SFR_{\mathrm{IR}}$. Dust attenuation was obtained from the ratio between L_{IR} and L_{UV} luminosities assuming the calibration of Buat et al. (2005). We stacked as a function of UV continuum slope, stellar mass, and dust attenuation. We only considered stacked detections with $f_{\mathrm{stack}} \geq 3\sigma_{\mathrm{stack}}$, where σ_{stack} is the uncertainty of each stacked flux. With the PACS data used in this work, stacked detections are only recovered for massive galaxies, typically with $\log(M_*/M_{\odot}) \gtrsim 10$. Therefore, we only studied a population of massive SF galaxies. Furthermore, although we considered galaxies up to $z \sim 4$, we only recovered stacked detections for galaxies at $z \leq 3$. Tables A.1 and A.2 summarize the stacked fluxes, rest-frame UV, and total IR luminosities, and the number of sources in each bin. We did not employ individual detections in our study since only the most extreme sources are detected with the depth of *Herschel* observations in COSMOS. They might not be normal SF galaxies, but most likely have a SB nature. The detection rate in *Herschel* bands is very low and, therefore, this does not change the main conclusions of our work.

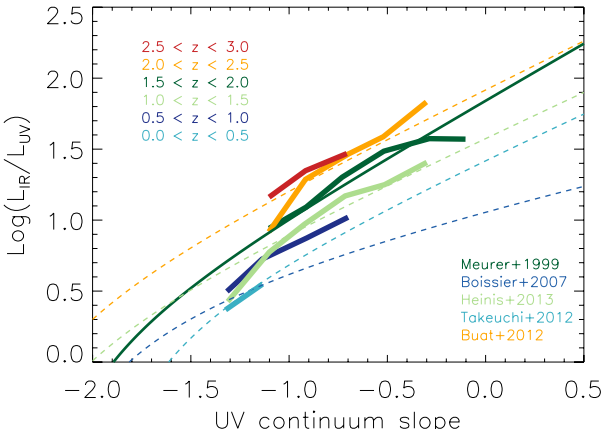

Fig. 1. Relation between the total IR and rest-frame UV luminosities (a proxy for dust attenuation) against the UV continuum slope as seen by our stacking analysis over $0.02 \lesssim z \lesssim 3.0$, with the color code shown in the top-left corner. We also represent the IRX-β relations reported in previous works (Meurer et al. 1999; Boissier et al. 2007; Heinis et al. 2013; Takeuchi et al. 2012; Buat et al. 2012), as indicated in the bottom-right corner. Their color code is related to the data they fit best.

3. Results

The relation between dust attenuation (parametrized by the $L_{\mathrm{IR}}/L_{\mathrm{UV}}$ ratio) against the UV continuum slope for our SF galaxies at different redshifts is shown in Fig. 1. At each redshift, redder galaxies are more attenuated. There is a clear trend with redshift for galaxies with $\beta \geq -1.0$: for a given UV continuum slope, galaxies at $z \sim 2$–3 are more attenuated than those at $z \sim 1$. This result is similar to the results found for individual detections in PACS/SPIRE (Oteo et al. 2013b,c, 2014), but now with a stacking analysis. This means that less dusty and IR-fainter galaxies can be probed at each epoch. At $z \lesssim 1$, where we can detect bluer galaxies, dust attenuation has not significantly changed with redshift for $\beta < -1.1$ SF galaxies. This might indicate that dust attenuation evolved only in massive, red SF galaxies, although deeper data are needed to confirm this.

These results confirm the evolution of the dust properties of massive SF galaxies over $0 < z < 3$. As a consequence of this evolutionary trend, there is not a single IRX-β relation that can be applied at all redshifts to accurately recover the dust attenuation or total SFR in massive SF galaxies. At low redshift, stacked points agree with the relation of Takeuchi et al. (2012), but the relation of Buat et al. (2012) should be applied at $z \sim 2$–3. We recall that at $z \sim 1.5$ our stacked points agree very well with the relation of Heinis et al. (2013), which was obtained with galaxies around that redshift through stacking in SPIRE bands.

As shown in Fig. 1, even with the stacking analysis in *Herschel*, we do not recover stacked detections for galaxies with $\beta \lesssim -1.3$ at any redshift (see also Heinis et al. 2013), nor with $\beta < -1.1$ at $z \geq 1.5$. This complicates testing the accuracy of the IRX-β relations at recovering dust attenuation because the SF galaxies selected in UV, optical, or NIR surveys have UV continuum slopes $\beta \lesssim -1.25$ in most cases (Oteo et al. 2013b,a, 2014). Therefore, a single IRX-β relation needs to be applied with care, because it has been shown here to evolve with redshift for massive, red ($\beta \geq -1.1$) SF galaxies and there is a complete lack of knowledge of its behavior at lower masses and bluer UV slope at different redshifts.

Figure 2 represents the dust attenuation in the FUV band (rest-frame 1500 Å) as a function of stellar mass for our SF galaxies at different redshifts. At a given redshift, more massive galaxies are more attenuated, as obtained in several previous

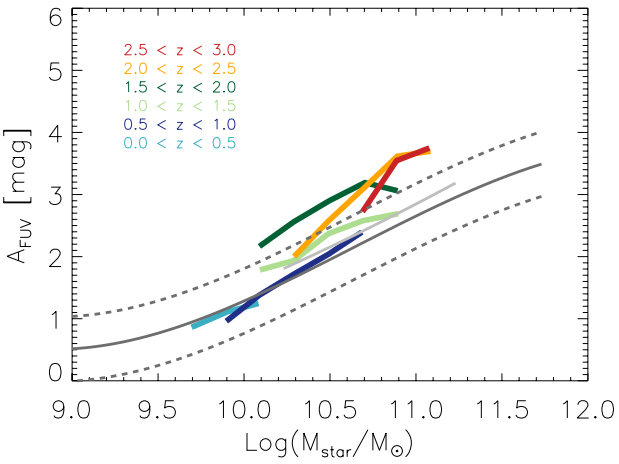

Fig. 2. Relation between dust attenuation and stellar mass for our stacked galaxies over $0.02 \lesssim z \lesssim 3.0$, with the color code shown in the top-left corner. The dust attenuation was derived with the $L_{\rm IR}/L_{\rm UV}$ ratio and the calibration of Buat et al. (2005). For reference, we represent the local relation as reported in Sobral et al. (2012) with a solid dark gray curve and the relation at $z \sim 1.5$ presented in Heinis et al. (2014) with a light gray solid line.

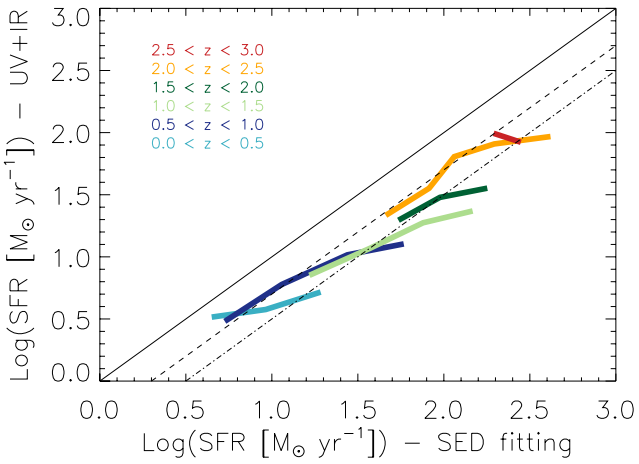

Fig. 3. Relation between the dust-corrected total SFRs derived with stacking analysis in PACS and from an SED fitting method assuming a constant SFR and fixed metallicity $Z = 0.2\ Z_{\odot}$. The one-to-one relation is shown with a black solid line, while deviations of −0.3 and −0.5 dex are indicated with dashed and dotted-dashed lines, respectively.

works (Ibar et al. 2013; Garn & Best 2010; Heinis et al. 2014). A trend with redshift is also present: massive ($\log(M_*/M_{\odot}) \geq 10$) galaxies at $z \sim 2$–3 were more attenuated for a given stellar mass than at $z \lesssim 1$. The relation reported by Heinis et al. (2014) is well recovered at the same redshift, $z \sim 1.5$. Since only galaxies with $\log(M_*/M_{\odot}) \geq 10$ have stacked detections at $z \geq 1$, we confirm the evolution in that mass range. At lower redshifts, where we can detect less massive galaxies, we find that the relation between dust attenuation and stellar mass agrees well with that found for local galaxies (Garn & Best 2010). This might indicate that the dust attenuation in less massive galaxies does not change significantly with redshift. This was obtained in Sobral et al. (2012) in Hα emitters (HAEs) at $z \sim 1.47$ and also with a stacking analysis in HAEs at the same redshift in Ibar et al. (2013). This result is important for recovering the dust attenuation or total SFR when FIR information is not available.

The power of the SED fitting method for recovering the total SFR in massive galaxies at $0 < z < 3$ is shown in Fig. 3. The points have been obtained by stacking as a function of the SED-derived dust attenuation, $E_{\rm s}(B-V)$. At any redshift, the SED-derived total SFR is systematically higher than those obtained from a stacking analysis. The overestimation is about 0.3–0.5 dex at all redshifts, but slightly higher for the galaxies with the highest SED-derived SFRs. At high redshift and for FIR-bright galaxies individually detected with PACS, the SED-derived total SFR underestimates the much more accurate SFR derived with direct UV and IR data (Wuyts et al. 2011). However, the stacking analysis presented here indicates that the SED-fitting method overestimates the total SFR at $0 < z < 3$ when galaxies with lower $L_{\rm IR}$ can be studied.

The relation between SFR and stellar mass for our stacked massive galaxies is shown in Fig. 4. Most previous works agree that there is a relation between SFR and stellar mass for normal SF galaxies, the so-called main sequence (MS, Daddi et al. 2007; Elbaz et al. 2007). Although there is much evidence that the MS exists, there is no consensus about its slope at different redshifts. This is mainly due to the different methods that can be employed to derive the stellar mass and total SFR of SF galaxies. Our stacking analysis reveals that the slope of the MS for massive ($\log(M_*/M_{\odot}) \geq 10$) SF galaxies is less stepper than previously reported (Elbaz et al. 2007; Daddi et al. 2007), mainly at our highest redshifts. We cannot detect less massive galaxies with stacking with the depths of the PACS images used here. Thus, it might be also possible that there is a break of the MS in massive galaxies, with the slope being steeper for galaxies with lower stellar masses and flatter for the most massive galaxies at each redshift (see also Whitaker et al. 2014, for an analysis with MIPS data). Deeper FIR data are needed to confirm this. The results shown in Heinis et al. (2014) also indicate that the slope of the MS might be lower for massive galaxies. These authors fit a linear relation to their points, although the points tend to follow the relation reported by Daddi et al. (2007) for their lowest massive galaxies and then the relation flattens at higher stellar masses. This flattening would agree with a break in the SFR-mass relation and is consistent with our results at the same redshift and across the same stellar mass range. At $z \sim 1$, our results agree with those of Rodighiero et al. (2010). At higher redshifts, Rodighiero et al. (2010) obtained stepper slopes, although their galaxies have bluer color than the studied in this work due to their selection criterion. It might be argued that the flattening of the MS at the highest redshifts is due to the presence of quiescent galaxies. Although we selected our galaxies for being SF according to their SFR, we have repeated the stacking when increasing the $\rm SFR_{UV}$ threshold to 5 $M_{\odot}\,{\rm yr}^{-1}$ for galaxies at $z \geq 1$ (again, before any dust correction, which means that the real SFR is even higher) to include only more active SF galaxies. It can be seen in Fig. 4 that even for these more active SF galaxies the slope of the MS is flatter than previously reported, suggesting that the flattening of the MS in massive galaxies is not caused by the presence of quiescent galaxies.

The redshift evolution of the specific SFR ($sSFR = SFR/M_{\odot}$) determined through stacking agree with previous compilations obtained with different methodologies, by increasing about one order of magnitude between $z \sim 0$ and $z \sim 2$. This is shown in the inset plot of Fig. 4.

4. Conclusions

By using a stacking analysis in *Herschel* bands, we have studied the accuracy of several dust-correction factors that are traditionally employed to recover the total SFR of high-redshift

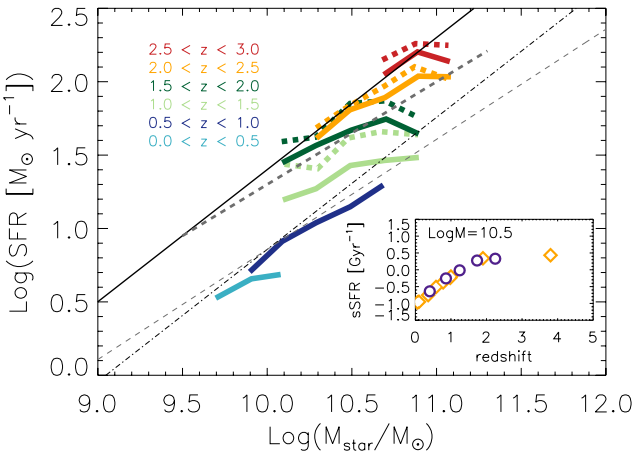

Fig. 4. Relation between $SFR = SFR_{\rm UV} + SFR_{\rm IR}$ and stellar mass for massive galaxies as revealed by our stacking analysis. We represent with dashed curves the points when the $\rm SFR_{UV}$ is limited to values higher than 5 $M_\odot\,{\rm yr}^{-1}$. The MS of Elbaz et al. (2007; black dotted-dashed line), Daddi et al. (2007; black solid line), and Heinis et al. (2014; thick grey dashed line) are included. We also show the MS with a slope of 0.75 and the same normalization of Daddi et al. (2007) to reflect the results of Rodighiero et al. (2010) at $z \lesssim 1$. We show in the bottom-right inset plot the evolution of the $sSFR = SFR/M_*$ for galaxies with $\log(M_*/M_\odot) \sim 10.5$. We also include the compilation of Dutton et al. (2010) with orange open squares.

star-forming (SF) galaxies. Our main conclusions are the following:

1. The dust attenuation in massive ($\log(M_*/M_\odot) > 10$) SF galaxies is higher at $z \sim 2$–3 than at $z \sim 1$ for a given UV continuum slope and stellar mass. This is consistent which what was previously found with individual *Herschel* detections. At $z \lesssim 1$, where stacking is able to detected less massive galaxies, we did not find significant evolution of dust attenuation for a given stellar mass compared with galaxies in the local Universe.
2. There is no single IRX-β relation that can be applied to accurately recover the dust attenuation or total SFR of massive SF galaxies at any redshift. Low-redshift galaxies are better parametrized by the relation of Takeuchi et al. (2012) IRX-β, but the relation reported by Buat et al. (2012) is more appropriate at $z \sim 2$. This might have implications for high-redshift studies, where a single IRX-β relation is normally assumed to correct for dust attenuation. The SED-derived dust attenuation gives overestimated total SFRs at all redshifts studied here.
3. Although the dust attenuation of massive galaxies is higher at $z \sim 2$–3 than at $z \sim 1$, our stacking analysis indicates that the local relation between dust attenuation and stellar mass is valid up to $z \sim 1$. Since we did not recover stacked detections at $z \geq 1.5$ for $\log(M_*/M_\odot) \lesssim 10$ galaxies, we cannot confirm the no evolution of the local dust-mass relation in low-mass galaxies at higher redshift reported in previous works.
4. We obtain that the slope of the MS of massive SF galaxies is lower than previously reported. Since we did not recover stacked detection for galaxies with $\log(M_*/M_\odot) \lesssim 10$, we cannot distinguish whether this is also true for less massive galaxies or if there is a break in the MS for massive galaxies. The redshift evolution of the sSFR agree with previous findings; it increased by about one order of magnitude from $z \sim 0.02$ to $z \sim 2$.

Acknowledgements. We acknowledge the anonymous referee for his/her report, which has improved the presentation of the results. I.O. acknowledges support from the European Research Council (ERC) in the form of Advanced Grant, COSMICISM. *Herschel* is an ESA space observatory with science instruments provided by European-led Principal Investigator consortia and with important participation from NASA. The *Herschel* spacecraft was designed, built, tested, and launched under a contract to ESA managed by the *Herschel*/Planck Project team by an industrial consortium under the overall responsibility of the prime contractor Thales Alenia Space (Cannes), and including Astrium (Friedrichshafen) responsible for the payload module and for system testing at spacecraft level, Thales Alenia Space (Turin) responsible for the service module, and Astrium (Toulouse) responsible for the telescope, with in excess of a hundred subcontractors. PACS has been developed by a consortium of institutes led by MPE (Germany) and including UVIE (Austria); KUL, CSL, IMEC (Belgium); CEA, OAMP (France); MPIA (Germany); IFSI, OAP/AOT, OAA/CAISMI, LENS, SISSA (Italy); IAC (Spain). This development has been supported by the funding agencies BMVIT (Austria), ESA-PRODEX (Belgium), CEA/CNES (France), DLR (Germany), ASI (Italy) and CICYT/MICINN (Spain).

References

Béthermin, M., Dole, H., Beelen, A., & Aussel, H. 2010, A&A, 512, A78
Béthermin, M., Le Floc'h, E., Ilbert, O., et al. 2012, A&A, 542, A58
Boissier, S., Le Floc'h, E., Ilbert, O., et al. 2007, ApJS, 173, 524
Bruzual, G., & Charlot, S. 2003, MNRAS, 344, 1000
Buat, V., Iglesias-Páramo, J., Seibert, M., et al. 2005, ApJ, 619, L51
Buat, V., Giovannoli, E., Burgarella, D., et al. 2010, MNRAS, 409, L1
Buat, V., Noll, S., Burgarella, D., et al. 2012, A&A, 545, A141
Calzetti, D., Armus L., Bohlin R. C., et al. 2000, ApJ, 533, 682
Chary, R., & Elbaz, D. 2001, ApJ, 556, 562
Daddi, E., Dickinson, M., Morrison, G., et al. 2007, ApJ, 670, 156
Dutton, A. A., van den Bosch, F. C., & Dekel, A. 2010, MNRAS, 405, 1690
Elbaz, D., Daddi, E., Le Borgne, D., et al. 2007, A&A, 468, 33
Elvis, M., Civano, F., Vignali, C., et al. 2009, ApJS, 184, 158
Feldmann, R., Carollo, C. M., Porciani, C., et al. 2006, MNRAS, 372, 565
Garn, T., & Best, P. N. 2010, MNRAS, 409, 421
Goldader, J. D., Meurer, G., Heckman, T. M., et al. 2002, ApJ, 568, 651
Heinis, S., Buat, V., Béthermin, M., et al. 2013, MNRAS, 429, 1113
Heinis, S., Buat, V., Béthermin, M., et al. 2014, MNRAS, 437, 1268
Ibar, E., Sobral, D., Best, P. N., et al. 2013, MNRAS, 434, 3218
Ilbert, O., McCracken, H. J., Le Fèvre, O., et al. 2013, A&A, 556, A55
Kennicutt, Jr. R. C. 1998, ARA&A, 36, 189
Madau, P. 1995, ApJ, 441, 18
Magdis, G. E., Elbaz, D., Hwang, H. S., et al. 2010, ApJ, 720, L185
Magnelli, B., Lutz, D., Saintonge, A., et al. 2014, A&A, 561, A86
Meurer, G. R., Heckman T. M., & Calzetti D. 1999, ApJ, 521, 64
Oke, J. B., Gunn, J. E. 1983, ApJ, 266, 713
Oteo, I., Bongiovanni, Á., Cepa, J., et al. 2013a, MNRAS, 433, 2706
Oteo, I., Cepa, J., Bongiovanni, Á., et al. 2013b, A&A, 554, L3
Oteo, I., Magdis, G., Bongiovanni, Á., et al. 2013c, MNRAS, 435, 158
Oteo, I., Bongiovanni, Á., Magdis, G., et al. 2014, MNRAS, 439, 1337
Pilbratt, G. L., Magdis, G., Bongiovanni, Á., et al. 2010, A&A, 518, L1
Poglitsch, A., Waelkens, C., Geis, N., et al. 2010, A&A, 518, L2
Rigopoulou, D., Magdis, G., Ivison, R. J., et al. 2010, MNRAS, 409, L7
Rodighiero, G., Magdis, G., Ivison, R. J., et al. 2010, A&A, 518, L25
Rodighiero, G., Renzini, A., Daddi, E., et al. 2014, MNRAS, 443, 19
Scoville, N., Aussel, H., Brusa, M., et al. 2007, ApJS, 172, 1
Sobral, D., Best, P. N., Matsuda, Y., et al. 2012, MNRAS, 420, 1926
Takeuchi, T. T., Yuan, F.-T., Ikeyama, A., Murata K. L., & Inoue, A. K. 2012, ApJ, 755, 144
Whitaker, K. E. Fraux, M., Leja, J., et al. 2014, ApJ, 795, 104
Williams, R. J., Quadri, R. F., Franx, M., van Dokkum, P., & Labbé, I. 2009, ApJ, 691, 1879
Wuyts, S., Förster Schreiber, N. M., Lutz, D., et al. 2011, ApJ, 738, 106
Zamojski, M. A., Schiminovich, D., Rich, R. M. et al. 2007, ApJS, 172, 468

Pages 5 to 12 are available in the electronic edition of the journal at http://www.aanda.org

Appendix A: Additional plots and tables

Table A.1. Summary of stacked properties when stacking as a function of the UV continuum slope.

Redshift range	UV slope range	$f_{160\ \mu m}$ [mJy]	$\log L_{UV}$	$\log L_{IR}$	N
$20.0 \leq z \leq 0.5$	$-1.4 \leq \beta \leq -1.2$	1.77 ± 0.19	9.61	9.98 ± 0.09	194
$20.0 \leq z \leq 0.5$	$-1.2 \leq \beta \leq -1.0$	2.73 ± 0.29	9.61	10.16 ± 0.09	121
$0.5 \leq z \leq 1.0$	$-1.4 \leq \beta \leq -1.2$	0.49 ± 0.04	9.72	10.22 ± 0.07	3125
$0.5 \leq z \leq 1.0$	$-1.2 \leq \beta \leq -1.0$	0.82 ± 0.06	9.72	10.44 ± 0.06	2064
$0.5 \leq z \leq 1.0$	$-1.0 \leq \beta \leq -0.8$	1.18 ± 0.08	9.73	10.60 ± 0.05	1244
$0.5 \leq z \leq 1.0$	$-0.8 \leq \beta \leq -0.6$	1.59 ± 0.10	9.70	10.72 ± 0.05	963
$1.0 \leq z \leq 1.5$	$-1.4 \leq \beta \leq -1.2$	0.18 ± 0.02	9.86	10.28 ± 0.09	8136
$1.0 \leq z \leq 1.5$	$-1.2 \leq \beta \leq -1.0$	0.41 ± 0.03	9.84	10.61 ± 0.06	5084
$1.0 \leq z \leq 1.5$	$-1.0 \leq \beta \leq -0.8$	0.65 ± 0.03	9.84	10.81 ± 0.04	4187
$1.0 \leq z \leq 1.5$	$-0.8 \leq \beta \leq -0.6$	0.97 ± 0.05	9.81	10.98 ± 0.05	2634
$1.0 \leq z \leq 1.5$	$-0.6 \leq \beta \leq -0.4$	1.16 ± 0.06	9.80	11.05 ± 0.04	1628
$1.0 \leq z \leq 1.5$	$-0.4 \leq \beta \leq -0.2$	1.54 ± 0.07	9.74	11.15 ± 0.04	1299
$1.5 \leq z \leq 2.0$	$-1.2 \leq \beta \leq -1.0$	0.42 ± 0.03	9.98	10.92 ± 0.05	4359
$1.5 \leq z \leq 2.0$	$-1.0 \leq \beta \leq -0.8$	0.56 ± 0.04	9.95	11.05 ± 0.06	3662
$1.5 \leq z \leq 2.0$	$-0.8 \leq \beta \leq -0.6$	0.77 ± 0.04	9.88	11.18 ± 0.05	2501
$1.5 \leq z \leq 2.0$	$-0.6 \leq \beta \leq -0.4$	1.01 ± 0.06	9.83	11.31 ± 0.05	1691
$1.5 \leq z \leq 2.0$	$-0.4 \leq \beta \leq -0.2$	1.08 ± 0.09	9.77	11.34 ± 0.07	1061
$1.5 \leq z \leq 2.0$	$-0.2 \leq \beta \leq -0.0$	1.11 ± 0.09	9.76	11.33 ± 0.06	825
$2.0 \leq z \leq 2.5$	$-1.2 \leq \beta \leq -1.0$	0.31 ± 0.05	10.21	11.13 ± 0.15	2041
$2.0 \leq z \leq 2.5$	$-1.0 \leq \beta \leq -0.8$	0.62 ± 0.06	10.13	11.43 ± 0.09	1470
$2.0 \leq z \leq 2.5$	$-0.8 \leq \beta \leq -0.6$	0.82 ± 0.09	10.07	11.53 ± 0.10	857
$2.0 \leq z \leq 2.5$	$-0.6 \leq \beta \leq -0.4$	0.73 ± 0.09	9.91	11.49 ± 0.10	776
$2.0 \leq z \leq 2.5$	$-0.4 \leq \beta \leq -0.2$	1.14 ± 0.12	9.86	11.69 ± 0.08	526
$2.5 \leq z \leq 3.0$	$-1.2 \leq \beta \leq -1.0$	0.47 ± 0.07	10.40	11.56 ± 0.15	1001
$2.5 \leq z \leq 3.0$	$-1.0 \leq \beta \leq -0.8$	0.58 ± 0.08	10.32	11.67 ± 0.13	721
$2.5 \leq z \leq 3.0$	$-0.8 \leq \beta \leq -0.6$	0.63 ± 0.13	10.22	11.69 ± 0.19	376

Notes. The uncertainties in the rest-frame UV luminosity are related to the normalization of the templates to the observed photometry; they are typically lower than 0.05 dex. The uncertainties in the total IR luminosities are obtained as the difference in the total IR luminosity when considering $f_{160\ \mu m} \pm \Delta f_{160\ \mu m}$. N indicates the number of galaxies in each bin.

Table A.2. Summary of stacked properties when stacking as a function of stellar mass.

Redshift range	Stellar mass range	$f_{160\ \mu m}$ [mJy]	$\log L_{UV}$	$\log L_{IR}$	N
$0.02 \leq z \leq 0.50$	$9.60 \leq \log(M_*/M_\odot) \leq 9.80$	1.39 ± 0.16	9.64	9.90 ± 0.10	184
$0.02 \leq z \leq 0.50$	$9.80 \leq \log(M_*/M_\odot) \leq 10.00$	2.18 ± 0.23	9.69	10.12 ± 0.09	170
$0.02 \leq z \leq 0.50$	$10.00 \leq \log(M_*/M_\odot) \leq 10.20$	2.55 ± 0.23	9.67	10.19 ± 0.07	111
$0.50 \leq z \leq 1.00$	$9.80 \leq \log(M_*/M_\odot) \leq 10.00$	0.42 ± 0.04	9.78	10.13 ± 0.10	2896
$0.50 \leq z \leq 1.00$	$10.00 \leq \log(M_*/M_\odot) \leq 10.20$	0.83 ± 0.05	9.83	10.46 ± 0.05	2246
$0.50 \leq z \leq 1.00$	$10.20 \leq \log(M_*/M_\odot) \leq 10.40$	1.30 ± 0.06	9.82	10.64 ± 0.04	1499
$0.50 \leq z \leq 1.00$	$10.40 \leq \log(M_*/M_\odot) \leq 10.60$	1.85 ± 0.09	9.79	10.79 ± 0.05	865
$0.50 \leq z \leq 1.00$	$10.60 \leq \log(M_*/M_\odot) \leq 10.80$	2.38 ± 0.11	9.77	10.98 ± 0.04	576
$1.00 \leq z \leq 1.50$	$10.00 \leq \log(M_*/M_\odot) \leq 10.20$	0.70 ± 0.04	9.95	10.81 ± 0.05	2877
$1.00 \leq z \leq 1.50$	$10.20 \leq \log(M_*/M_\odot) \leq 10.40$	0.90 ± 0.05	9.97	10.90 ± 0.04	2101
$1.00 \leq z \leq 1.50$	$10.40 \leq \log(M_*/M_\odot) \leq 10.60$	1.41 ± 0.06	9.93	11.10 ± 0.03	1541
$1.00 \leq z \leq 1.50$	$10.60 \leq \log(M_*/M_\odot) \leq 10.80$	1.64 ± 0.10	9.87	11.15 ± 0.05	1152
$1.00 \leq z \leq 1.50$	$10.80 \leq \log(M_*/M_\odot) \leq 11.00$	1.71 ± 0.10	9.83	11.18 ± 0.05	869
$1.50 \leq z \leq 2.00$	$10.00 \leq \log(M_*/M_\odot) \leq 10.20$	0.62 ± 0.05	10.04	11.11 ± 0.06	2688
$1.50 \leq z \leq 2.00$	$10.20 \leq \log(M_*/M_\odot) \leq 10.40$	0.85 ± 0.06	9.98	11.25 ± 0.06	1682
$1.50 \leq z \leq 2.00$	$10.40 \leq \log(M_*/M_\odot) \leq 10.60$	1.13 ± 0.08	9.93	11.37 ± 0.06	1158
$1.50 \leq z \leq 2.00$	$10.60 \leq \log(M_*/M_\odot) \leq 10.80$	1.33 ± 0.10	9.89	11.46 ± 0.06	851
$1.50 \leq z \leq 2.00$	$10.80 \leq \log(M_*/M_\odot) \leq 11.00$	1.08 ± 0.12	9.83	11.35 ± 0.09	656
$2.00 \leq z \leq 2.50$	$10.20 \leq \log(M_*/M_\odot) \leq 10.40$	0.40 ± 0.05	10.27	11.26 ± 0.12	2083
$2.00 \leq z \leq 2.50$	$10.40 \leq \log(M_*/M_\odot) \leq 10.60$	0.70 ± 0.07	10.21	11.50 ± 0.09	1514
$2.00 \leq z \leq 2.50$	$10.60 \leq \log(M_*/M_\odot) \leq 10.80$	0.90 ± 0.08	10.06	11.60 ± 0.07	984
$2.00 \leq z \leq 2.50$	$10.80 \leq \log(M_*/M_\odot) \leq 11.00$	1.32 ± 0.12	9.976	11.76 ± 0.07	616
$2.00 \leq z \leq 2.50$	$11.00 \leq \log(M_*/M_\odot) \leq 11.20$	1.30 ± 0.15	9.90	11.76 ± 0.09	389
$2.50 \leq z \leq 3.00$	$10.60 \leq \log(M_*/M_\odot) \leq 10.80$	0.69 ± 0.10	10.38	11.75 ± 0.12	645
$2.50 \leq z \leq 3.00$	$10.80 \leq \log(M_*/M_\odot) \leq 11.00$	1.05 ± 0.13	10.16	11.93 ± 0.11	418
$2.50 \leq z \leq 3.00$	$11.00 \leq \log(M_*/M_\odot) \leq 11.20$	0.90 ± 0.17	10.04	11.87 ± 0.16	197

Notes. The uncertainties in the rest-frame UV luminosity are related to the normalization of the templates to the observed photometry; they are typically lower than 0.05 dex. The uncertainties in the total IR luminosities are obtained as the difference in the total IR luminosity when considering $f_{160\ \mu m} \pm \Delta f_{160\ \mu m}$. N indicates the number of galaxies in each bin.

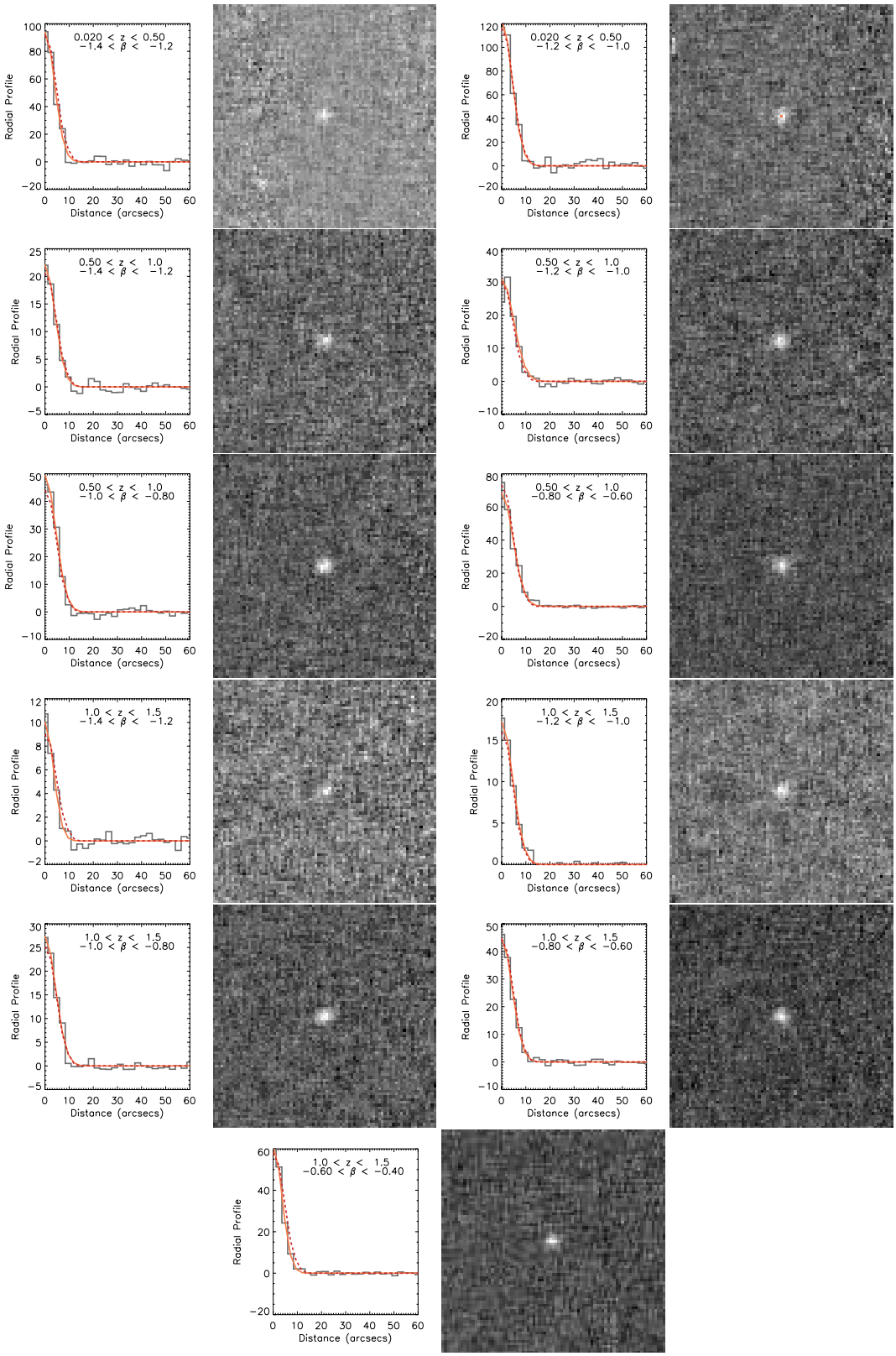

Fig. A.1. Radial profiles and associated stacked images when stacking as a function of the UV continuum slope. Redshift and UV continuum bins are indicated in each case. Orange curves are the best-fit Gaussian to the radial profile, while red dashed curves represent the shape of the PACS-160 μm PSF.

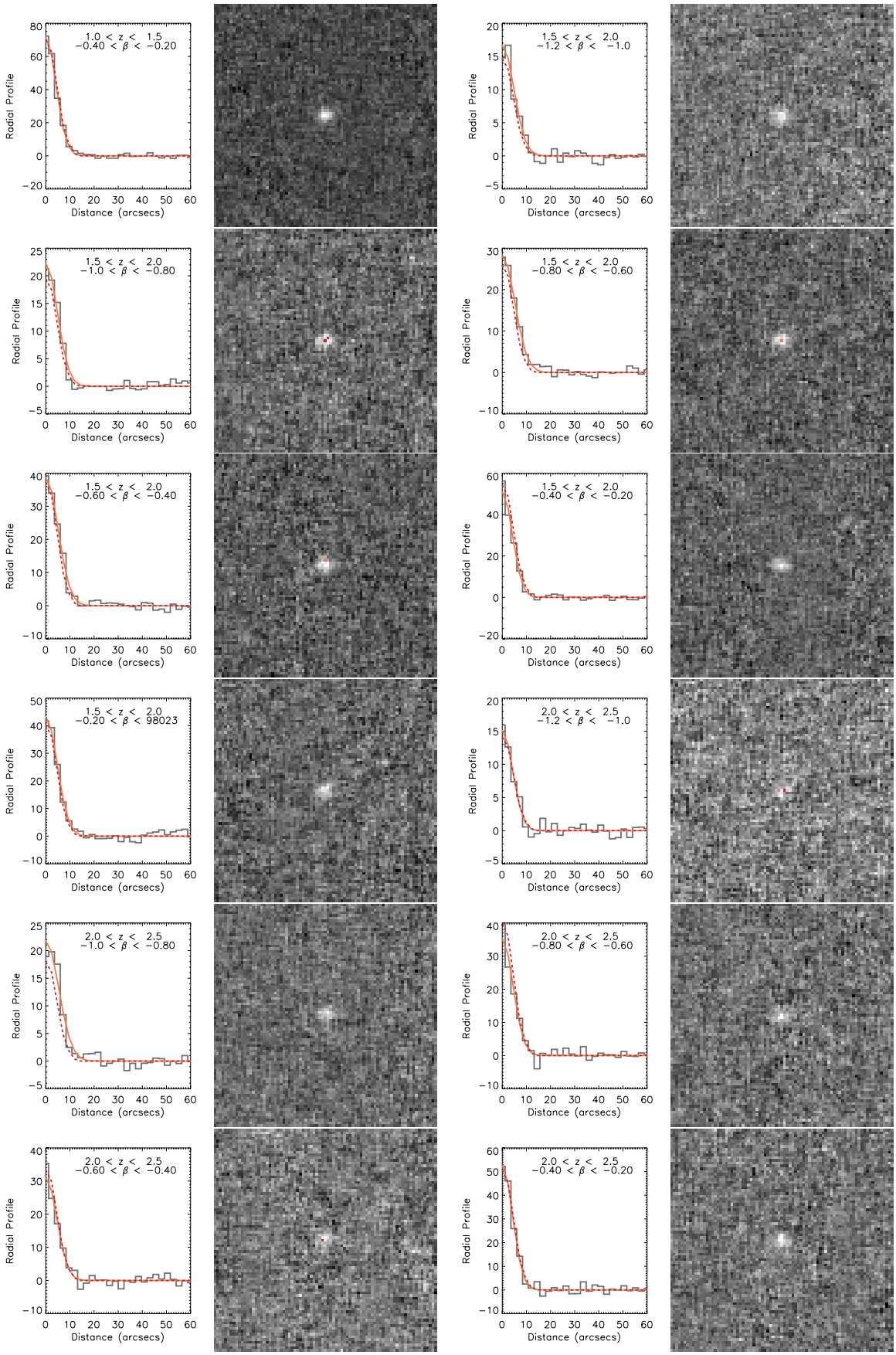

Fig. A.1. continued.

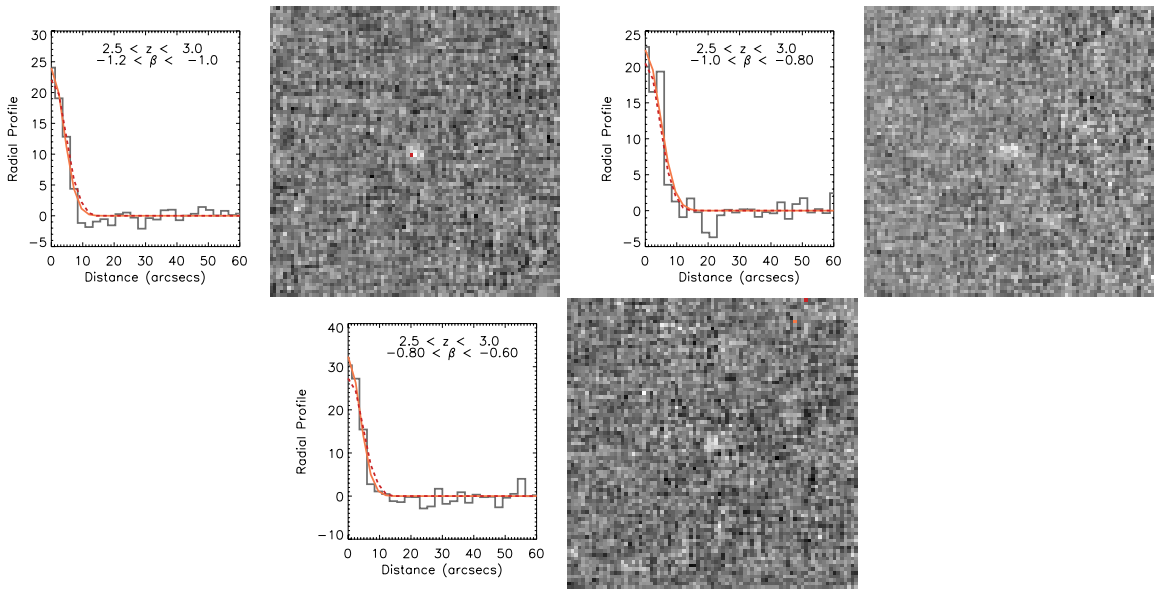

Fig. A.1. continued.

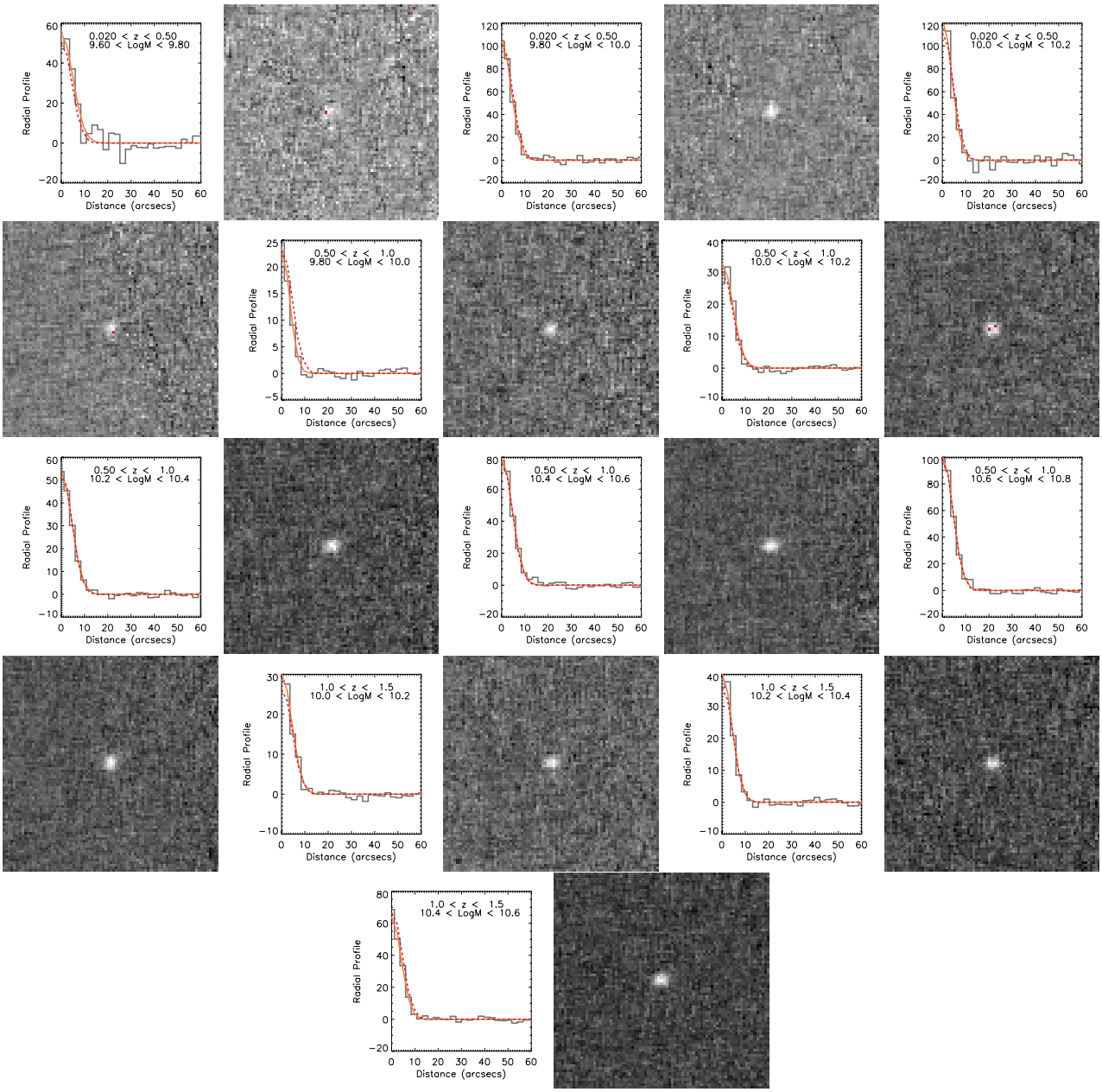

Fig. A.2. Radial profiles and associated stacked images when stacking as a function of the stellar mass. Redshift and stellar mass bins are indicated in each case. Orange curves are the best-fitted Gaussian to the radial profile, while red dashed curves represent the shape of the PACS-160 μm PSF.

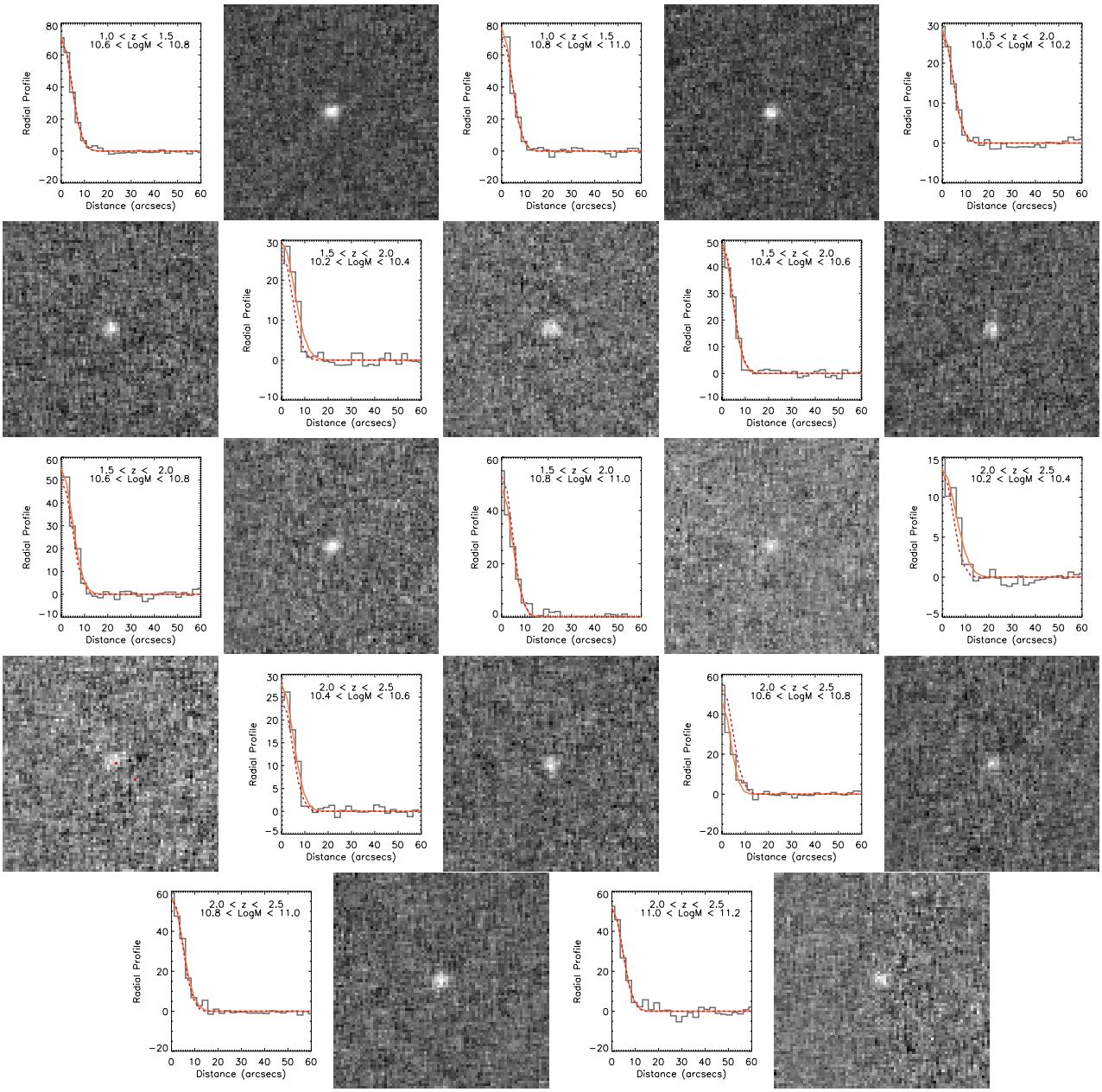

Fig. A.2. continued.

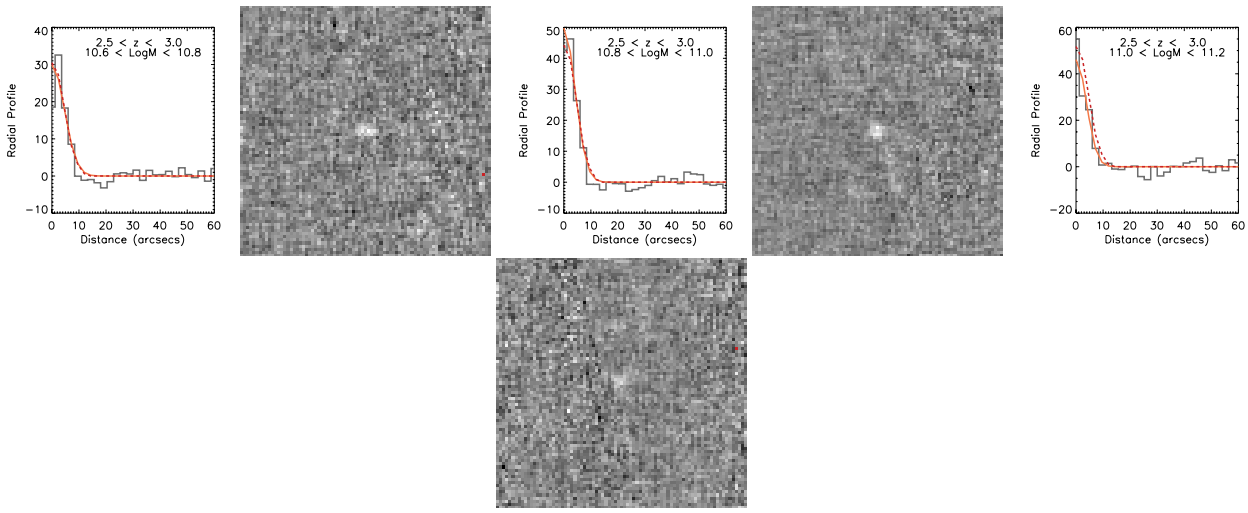

Fig. A.2. continued.